



HAL
open science

Flight control of a balloon-hexacopter: uncertainty quantification for a range of temperature and pressure conditions

Davi Antonio Santos, Americo Cunha Jr

► **To cite this version:**

Davi Antonio Santos, Americo Cunha Jr. Flight control of a balloon-hexacopter: uncertainty quantification for a range of temperature and pressure conditions. 2017. hal-01541169v1

HAL Id: hal-01541169

<https://hal.science/hal-01541169v1>

Preprint submitted on 18 Jun 2017 (v1), last revised 12 Sep 2019 (v2)

HAL is a multi-disciplinary open access archive for the deposit and dissemination of scientific research documents, whether they are published or not. The documents may come from teaching and research institutions in France or abroad, or from public or private research centers.

L'archive ouverte pluridisciplinaire **HAL**, est destinée au dépôt et à la diffusion de documents scientifiques de niveau recherche, publiés ou non, émanant des établissements d'enseignement et de recherche français ou étrangers, des laboratoires publics ou privés.

Copyright

Flight Control of a Balloon-Hexacopter: Uncertainty Quantification for a Range of Temperature and Pressure Conditions

Davi Antonio dos Santos^a, Americo Cunha Jr^b

^a*Aeronautics Institute of Technology, São José dos Campos, Brazil*

^b*Rio de Janeiro State University, Rio de Janeiro, Brazil*

Abstract

The present paper is concerned with the dynamic modeling as well as the design of position and attitude control laws for a balloon-multicopter aerial vehicle consisting of an oblate spheroid helium balloon coupled with a hexacopter airframe. A six-degrees-of-freedom nonlinear dynamic model is derived for the balloon-hexacopter using the Newton-Euler approach and considering, among other common efforts, a restoration torque due to the displacement of the balloon's center of buoyancy above the vehicle's center of mass. Under the assumption of time-scale separation between the translational and rotational dynamics, the attitude and position control laws are designed separately from each other. Both controllers are proportional-derivative actions plus nonlinear feedforward terms for feedback linearization combined with control input saturation within appropriate parallelepipedal sets, which are carefully chosen to respect pre-defined bounds on the control torque, control force and inclination angle. The proposed flight control system is evaluated under different local temperature and pressure conditions. In particular, both parameters are modeled as uniformly-distributed random variables and the system responses are investigated using the Monte Carlo stochastic solver. Extensive simulation results show the effectiveness of the proposed control system and quantifies the uncertainty of its performance over a wide range of local temperature and pressure.

Keywords: Balloon-multicopter, multicopter aerial vehicle, flight control system, uncertainty quantification.

1. Introduction

In the last few years, the multirotor aerial vehicles (MAVs) have found many applications, including small package delivering, precise agriculture monitoring, surveillance in urban areas, building inspections, just to cite a few. In most cases, the operation could become more effective and efficient if the flight duration and payload capacity were extended. A very simple way to improve an MAV in these two aspects is by combining it with a helium balloon that provides a net aerostatic lift counteracting the total weight of the vehicle. In general, we name such a combination as a balloon-multicopter. The balloon-multicopter considered in this paper is depicted in Figure 1. It consists of an oblate spheroid balloon filled with helium attached to a hexacopter airframe. These two parts are strapped down at six points by ropes. The balloon is made on polyurethane and has 2.5 m of diameter and 1.6 m of height. With a payload of 4.42 kg, the vehicle has a buoyancy ratio of 0.7 and, to not exceed the maximum bounds of approximately 12 Nm in the horizontal torque, the attitude control must maintain the vehicle's inclination angle below 15 degrees.

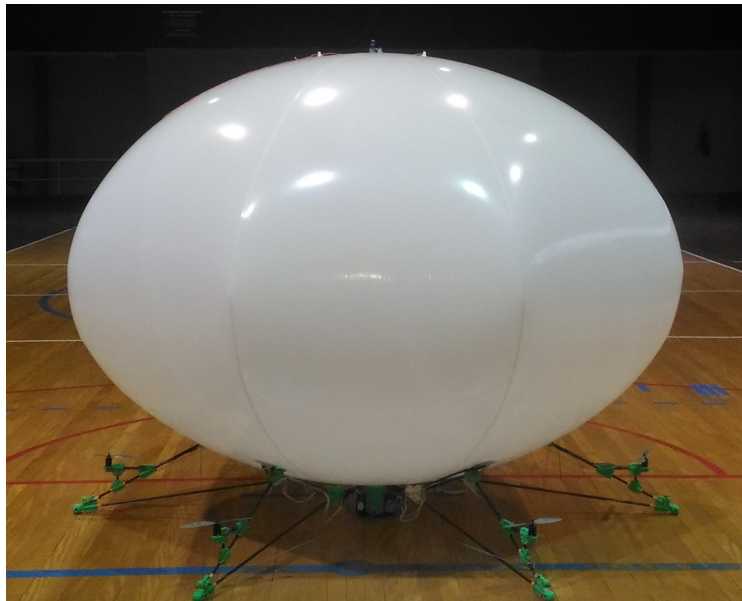


Figure 1: The balloon-hexacopter of the LRA-ITA (www.lra.ita.br).

Besides the aforementioned advantages of the new aerial vehicle over the MAVs, one can also highlight its simplicity compared to other vehicles with good payload and flight duration capabilities, such as the blimps and the conventional fuel-engine helicopters. The former has a more

complex construction that includes vectoring rotors and aerodynamic surfaces, while the latter requires elaborated mechanical linkages and a swashplate.

The design of a control system for a balloon-multicopter, even if it is intended to operate indoors with low speed, presents a critical challenge due to the restoring torque generated by the displacement of the balloon's center of buoyancy (CB) above the vehicle's center of mass (CM). For a fixed CB-CM displacement, the larger the inclination angle of the vehicle with respect to the local vertical, the larger the magnitude of the restoring torque. Therefore, for a given design of the rotor set, the attitude controller must respect a maximum bound on the inclination angle for the control system to maintain its effectiveness. The side effect of this constraint is usually a low lateral acceleration capability. Another important challenge is related to the unpredictability of the local temperature and pressure for the operation of vehicle. Changes in these parameters can cause severe variabilities in air and helium density. As a consequence, the balloon's aerostatic lift and restoring torque also suffer a variation, which can directly impact on the control system performance. A systematic evaluation of the effects of these uncertainties on the system dynamics is essential as a preliminary analysis for a posterior robust design of the flight control system.

A vast literature on the design of control laws for conventional MAVs, in special for quadcopters, has emerged in the last ten years thanks to the popularization of such vehicles and motivated by the reasonable control challenge it poses. The dynamics of such vehicles has six degrees of freedom (DOFs) – three in translation and three others in rotation – but, on the other hand, has only four control inputs (thrust magnitude and three orthogonal torque components). This under-actuation characteristic does not complicate the control since one is often interested in tracking only four DOFs independently (three orthogonal position components and heading). Moreover, the MAV flight dynamics is inherently nonlinear, but for slow flights it can be approximately modeled by a linear time-invariant model. A nice introduction to the control of MAVs can be found in the reference [1].

The most common flight control architecture adopted not only in MAVs but in aerospace vehicles in general is an hierarchical control scheme in which the inner loop is concerned with the attitude control, while the outer loop realizes the position control. In this strategy, the inner loop must be supposed to have a much faster dynamics than the outer loop. This is the well-

known time-scale separation assumption [2]. The literature contains many different methods for designing attitude and position controllers for MAVs. The early works used linear design methods, such as PID and LQR, on the basis of linearized and decoupled models of the MAV translational and rotational dynamics [3, 4]. Such methods showed effective only in bench experiments and simulations in which the vehicles were supposed to be near the hovering conditions.

In order to allow for faster dynamics, nonlinear control strategies appeared in [5, 6, 7, 8]. The reference [5] designs a PD-like quaternion-based nonlinear attitude controller with feedback compensation of the Coriolis and gyroscopic torques for a quadcopter. The overall system is shown to be exponentially stable at the origin. The reference [6] uses the backstepping procedure to derive a nonlinear control law that assures asymptotic stability of the position tracking error at the origin. The resulting control law is inconvenient to implement, since it depends on the fourth-order derivative of the position command and on the first-order derivative of the thrust command. The reference [7] proposes a nonlinear geometric attitude and position controller for a quadcopter on $SE(3)$ and shows that the closed-loop system is exponentially stable. Finally, the reference [8] proposes a PD-like law with nonlinear feedback linearization for the position dynamics of a multicopter. In particular, it imposes bounds on the thrust vector command both in magnitude and inclination with respect to the local vertical. The satisfaction of such control bounds is also accomplished in [9], using a model predictive controller (MPC), as well as in [10], using the retrospective cost adaptive controller (RCAC).

After about 2012, the MAV literature starts to worry about robustness with respect to parameter uncertainty and unknown force and torque disturbances [11, 12, 13, 14]. The reference [11] uses a sliding mode control in combination with a sliding mode disturbance observer to design a robust flight controller for a quadcopter subject to external disturbances and model uncertainties. The reference [12] proposes an extension of the work presented in [7] for systems subject to bounded disturbance torque and force. It designs attitude and position controllers in $SE(3)$ based on the time-scale separation assumption and shows that the control errors are uniformly ultimately bounded. The reference [13] adopts a second-order sliding mode control method to design an attitude and a position controller for a quadcopter under force and torque disturbances. For tuning the coefficient of the sliding surfaces, it uses linear stability concepts. Finally, the reference

[14] designed attitude and altitude control laws for a quadcopter subject to disturbance, using an adaptive sliding mode control strategy in which the sliding boundary is adjusted on-line based on disturbance estimates provided by a high-gain observer.

The present paper is concerned with the dynamic modeling and design of flight control laws for a hybrid unmanned aerial vehicle (UAV) consisting of an oblate spheroid helium balloon coupled with a multicopter airframe containing six vertical fixed rotors. A nonlinear six DOF dynamic model is derived for this balloon-hexacopter using the Newton-Euler approach. Among other efforts to which the conventional MAVs are usually subject, the proposed model includes a restoring torque that stems from the displacement of the balloon's CB above the vehicle's CM. The most common flight control framework in aerospace systems is adopted here. It is a hierarchical architecture, based on the so-called time-scale separation assumption, in which the attitude control is realized by an inner loop while the position control is carried out by an outer loop. In this way, the attitude and position control laws are separately designed using feedback linearization and considering the saturation of the control vector within appropriate parallelepipedal sets that ensure the satisfaction of design bounds on the control torque and force, as well as on the vehicle's inclination angle. The remaining text is organized in the following manner. Section 2 derives a six-DOF dynamic model for the balloon-hexacopter. Section 3 is concerned with the design of the nonlinear attitude and position control laws. Section 4 evaluates the proposed control system in a deterministic scenario. Section 5 carries out a stochastic uncertainty quantification analysis of the system considering a random variation of both the local temperature and pressure conditions over wide but known ranges. Finally, Section 6 concludes the paper.

2. Dynamic Modeling

This section derives the rotational and translational equations of motion and actuator models for the balloon-hexacopter under consideration. We start with preliminary definitions in Subsection 2.1, then we model the rotor dynamics and control efforts in Subsection 2.2, the restoring torque and aerostatic lift generated by the balloon in Subsection 2.3, the vehicle's rotational dynamics in Subsection 2.4, and its translational dynamics in Subsection 2.5.

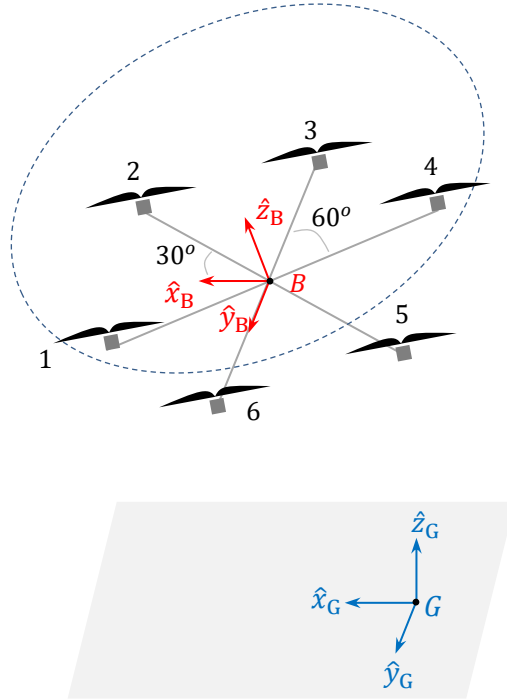


Figure 2: The Cartesian coordinate systems (CCS). $S_B = \{\hat{x}_B, \hat{y}_B, \hat{z}_B\}$ is the body CCS and $S_G = \{\hat{x}_G, \hat{y}_G, \hat{z}_G\}$ is the ground CCS.

2.1. Preliminary definitions

We define two Cartesian coordinate systems (CCS) as illustrated in Figure 2. The body CCS, $S_B \triangleq \{\hat{x}_B, \hat{y}_B, \hat{z}_B\}$ is attached to the vehicle's body with the origin at the vehicle's center of mass B , the \hat{x}_B axis is pointing forward, aligned with the bisectrix of the separation angle between the rotors 1 and 2, the \hat{z}_B axis is pointing upward, normal to the rotor plane, and the \hat{y}_B axis completes a right-handed coordinate system. The ground CCS, $S_G \triangleq \{\hat{x}_G, \hat{y}_G, \hat{z}_G\}$ is fixed to the ground at a known point G , with the \hat{z}_G axis pointing upward vertically. For our purposes, S_G can be considered as an inertial frame.

The notation adopted here distinguishes between two kinds of vectors: physical vectors and algebraic vectors. Physical vectors are denoted by lowercase italic letters with a right arrow superscript, *e.g.*, \vec{r} . The corresponding algebraic vector, resulting from the projection of \vec{r} onto an arbitrary CCS S_A is denoted by a lowercase boldface letter with the subscript A, *i.e.*, $\mathbf{r}_A \in \mathbb{R}^3$. The text will often refer to \mathbf{r}_A as the S_A representation of \vec{r} . Now consider a relative vector physical

quantity \vec{a} (such as position or velocity) of the CCS S_A with respect to another CCS S_B . In this case, we would better explicitly denote this physical vector by $\vec{a}^{A/B}$ and its S_A and S_B representations by $\mathbf{a}_A^{A/B}$ and $\mathbf{a}_B^{A/B}$, respectively. The attitude of S_A w.r.t. S_B is fundamentally represented by the attitude matrix $\mathbf{D}^{A/B} \in \text{SO}(3)$; consider the physical vector \vec{r} and its representations \mathbf{r}_A and \mathbf{r}_B . The attitude matrix $\mathbf{D}^{A/B}$ is such that $\mathbf{r}_A = \mathbf{D}^{A/B}\mathbf{r}_B$.

Consider two algebraic vectors $\mathbf{a} = [a_1 \ a_2 \ a_3]^T$ and \mathbf{b} . We denote the vector product between them by the matrix multiplication $[\mathbf{a} \times] \mathbf{b}$, where $[\mathbf{a} \times]$ is a skew-symmetric matrix

$$[\mathbf{a} \times] \triangleq \begin{bmatrix} 0 & -a_3 & a_2 \\ a_3 & 0 & -a_1 \\ -a_2 & a_1 & 0 \end{bmatrix}. \quad (1)$$

2.2. Rotor Dynamics and Efforts

The set of six rotors equipping the airframe is responsible for generating the control forces and torques as described here. The i th rotor individually produces a thrust force and a reaction torque on the airframe along the \hat{z}_B axis with magnitudes denoted by f_i and τ_i , respectively. We describe these efforts by the following aerodynamic models:

$$f_i = k_f \omega_i^2, \quad (2)$$

$$\tau_i = k_\tau \omega_i^2, \quad (3)$$

$i = 1, \dots, 4$, where k_f is the thrust force coefficient, k_τ is the reaction torque coefficient, and ω_i is the rotation speed of the i th rotor. The rotor dynamics can be modeled by the following first-order linear model:

$$\dot{\omega}_i = -\frac{1}{\tau_\omega} \omega_i + \frac{k_\omega}{\tau_\omega} \bar{\omega}_i, \quad (4)$$

where $\bar{\omega}_i \in [0, \bar{\omega}_{\max}]$ is the rotation speed command of the i th rotor, k_ω is the speed coefficient, and τ_ω is the rotor time constant. The rotation bound $\bar{\omega}_{\max}$ is assumed to be known.

Consider that all the six thrusts f_i point upward. Moreover, consider that the reaction torque

τ_1 is positive, τ_2 is negative, τ_3 is positive, and so on. Therefore, one can show that the magnitude F^c of the resulting control force and the S_B representation \mathbf{T}_B^c of the resulting control torque are given by

$$\begin{bmatrix} F^c \\ \mathbf{T}_B^c \end{bmatrix} = \mathbf{\Gamma} \mathbf{f}, \quad (5)$$

where $\mathbf{f} \triangleq [f_1 \ f_2 \ \dots \ f_6]^T$ and

$$\mathbf{\Gamma} \triangleq \begin{bmatrix} 1 & 1 & 1 & 1 & 1 & 1 \\ 0 & -l\sqrt{3}/2 & -l\sqrt{3}/2 & 0 & l\sqrt{3}/2 & l\sqrt{3}/2 \\ -l & -l/2 & l/2 & l & l/2 & -l/2 \\ k & -k & k & -k & k & -k \end{bmatrix} \in \mathbb{R}^{4 \times 6}, \quad (6)$$

where l is the length of each vehicle's arm, and $k \triangleq k_\tau/k_f$.

2.3. Aerostatic Lift and Restoring Torque

This subsection models two crucial efforts generated by the balloon. One is an aerostatic lift force \vec{F}^b and the other one is a restoring torque \vec{T}^b . The force \vec{F}^b is explained by the Archimedes' Principle, which says that it always points upwards parallel to the local vertical and its magnitude is equal to the weight of the air volume displaced by the balloon minus the weight of the lifting gas (the helium) itself. Therefore, one can immediately write the S_G representation of \vec{F}^b as

$$\mathbf{F}_G^b = \begin{bmatrix} 0 \\ 0 \\ Vg(\rho_{\text{air}} - \rho_{\text{helium}}) \end{bmatrix}, \quad (7)$$

where V is the volume of the balloon, g is the gravitational acceleration, ρ_{air} is the air density, and ρ_{helium} is the helium density.

On the other hand, the restoring torque \vec{T}^b is an effort acting about the vehicle's CM, which appears as a consequence of the displacement d between the balloon's CB and the vehicle's CM.

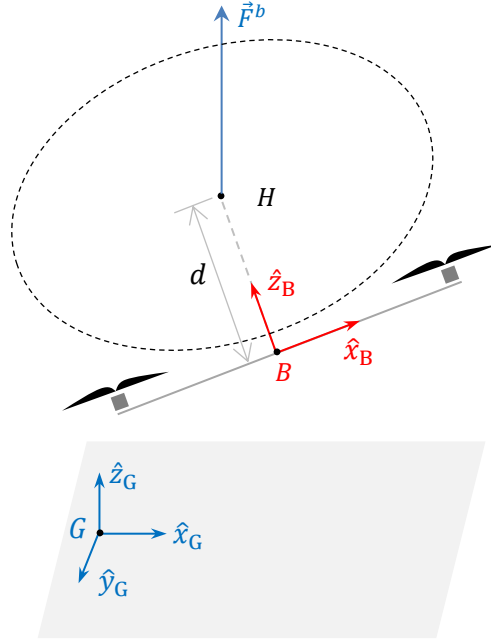


Figure 3: The restoring torque.

Figure 3 illustrate the balloon-airframe connection, which is assumed here to be rigid. In this case, the CB, which is placed at point H , is fixed w.r.t. S_B . From the illustration, one can immediately write

$$\vec{T}^b = (d\hat{z}_B) \times \vec{F}^b. \quad (8)$$

By representing (projecting) equation (8) in S_B , we finally have

$$\mathbf{T}_B^b = [(d\mathbf{e}_3) \times] \mathbf{D}^{B/G} \begin{bmatrix} 0 \\ 0 \\ F^b \end{bmatrix}, \quad (9)$$

where $\mathbf{D}^{B/G}$ is the attitude matrix of S_B w.r.t. S_G and $F^b \triangleq Vg(\rho_{\text{air}} - \rho_{\text{helium}})$ is the magnitude of \vec{F}^b .

2.4. Rotational Motion

The kinematics equation of the rotational motion of S_B w.r.t. S_G is given in $\text{SO}(3)$ by

$$\dot{\mathbf{D}}^{\text{B/G}} = - \left[\boldsymbol{\Omega}_{\text{B}}^{\text{B/G}} \times \right] \mathbf{D}^{\text{B/G}}, \quad (10)$$

where $\boldsymbol{\Omega}_{\text{B}}^{\text{B/G}}$ is the S_{B} representation of the vehicle's angular velocity w.r.t. S_{G} .

Assume that the vehicle has a rigid structure and S_{G} is an inertial frame. Therefore, the Second Euler's Law allows

$$\dot{\mathbf{H}}_{\text{B}} + \left[\boldsymbol{\Omega}_{\text{B}}^{\text{B/G}} \times \right] \mathbf{H}_{\text{B}} = \mathbf{T}_{\text{B}}^{\text{c}} + \mathbf{T}_{\text{B}}^{\text{b}} + \mathbf{T}_{\text{B}}^{\text{d}}, \quad (11)$$

where \mathbf{H}_{B} is the S_{B} representation of the total angular momentum of the vehicle, $\mathbf{T}_{\text{B}}^{\text{c}}$ is the S_{B} representation of the control torque (see equation (5)), $\mathbf{T}_{\text{B}}^{\text{d}}$ is the S_{B} representation of the (unknown) disturbance torque, and $\mathbf{T}_{\text{B}}^{\text{b}}$ is the S_{B} representation of the balloon restoring torque (see Subsection 2.3).

Considering the rotation of both the body and the propellers and noting that the latter rotates much faster, the total angular momentum \mathbf{H}_{B} can be written as

$$\mathbf{H}_{\text{B}} = \mathbf{J}^{\text{b}} \boldsymbol{\Omega}_{\text{B}}^{\text{B/G}} + J^{\text{r}} \sum_{i=1}^6 (-1)^i \omega_i \mathbf{e}_3, \quad (12)$$

where $\mathbf{J}^{\text{b}} \in \mathbb{R}^{3 \times 3}$ is the inertia matrix of the vehicle and $J^{\text{r}} \in \mathbb{R}$ is the moment of inertia of the rotors about \hat{z}_{B} .

Therefore, by replacing equation (12) into equation (11), one can obtain the dynamic equation of the rotational motion of S_{B} w.r.t. S_{G} with vectors represented in S_{B} :

$$\dot{\boldsymbol{\Omega}}_{\text{B}}^{\text{B/G}} = (\mathbf{J}^{\text{b}})^{-1} \left(\left[\left(\mathbf{J}^{\text{b}} \boldsymbol{\Omega}_{\text{B}}^{\text{B/G}} + J^{\text{r}} \sum_{i=1}^6 (-1)^i \omega_i \mathbf{e}_3 \right) \times \right] \boldsymbol{\Omega}_{\text{B}}^{\text{B/G}} - J^{\text{r}} \sum_{i=1}^6 (-1)^i \dot{\omega}_i \mathbf{e}_3 + \mathbf{T}_{\text{B}}^{\text{b}} + \mathbf{T}_{\text{B}}^{\text{c}} + \mathbf{T}_{\text{B}}^{\text{d}} \right). \quad (13)$$

2.5. Translational Motion

By invoking the Second Newton's Law considering all the vectors represented in S_{G} , one can immediately write

$$\mathbf{M}\ddot{\mathbf{r}}_G^{\text{B/G}} = \mathbf{F}_G^g + \mathbf{F}_G^b + \mathbf{F}_G^c + \mathbf{F}_G^d, \quad (14)$$

$$\mathbf{M} \triangleq m^t \mathbf{I}_3 + \begin{bmatrix} m^h \mathbf{I}_2 & \mathbf{0}_{2 \times 1} \\ \mathbf{0}_{1 \times 2} & 0 \end{bmatrix}, \quad (15)$$

where m^t is the total mass of the vehicle without lifting gas and including the payload, $m^h = \rho_{\text{helium}} V$ is the helium mass, $\mathbf{r}_G^{\text{B/G}} \in \mathbb{R}^3$ is the S_G representation of the position of the vehicle's center of mass B w.r.t. G , \mathbf{F}_G^g is the S_G representation of the gravitational force, \mathbf{F}_G^b is the S_G representation of the balloon aerostatic lift force, \mathbf{F}_G^c is the S_G representation of the control force, and \mathbf{F}_G^d is the S_G representation of the (unknown) disturbance force. The force \mathbf{F}_G^b is given by equation (7), while \mathbf{F}_G^g and \mathbf{F}_G^c are modeled by

$$\mathbf{F}_G^g = \begin{bmatrix} 0 \\ 0 \\ -m^t g \end{bmatrix} \quad \text{and} \quad \mathbf{F}_G^c = \left(\mathbf{D}^{\text{B/G}} \right)^T \begin{bmatrix} 0 \\ 0 \\ F^c \end{bmatrix}. \quad (16)$$

By replacing equations (15)-(16) into (14), we finally obtain the dynamic model for the translational motion

$$\ddot{\mathbf{r}}_G^{\text{B/G}} = F^c \mathbf{M}^{-1} \mathbf{n}_G + \begin{bmatrix} 0 \\ 0 \\ Vg(\rho_{\text{air}} - \rho_{\text{helium}})/m^t - g \end{bmatrix} + \mathbf{M}^{-1} \mathbf{F}_G^d, \quad (17)$$

where $\mathbf{n}_G \in \mathbb{R}^3$ is the transpose of the third line of $\mathbf{D}^{\text{B/G}}$, which corresponds to the S_G representation of the unit vector normal to the rotor plane.

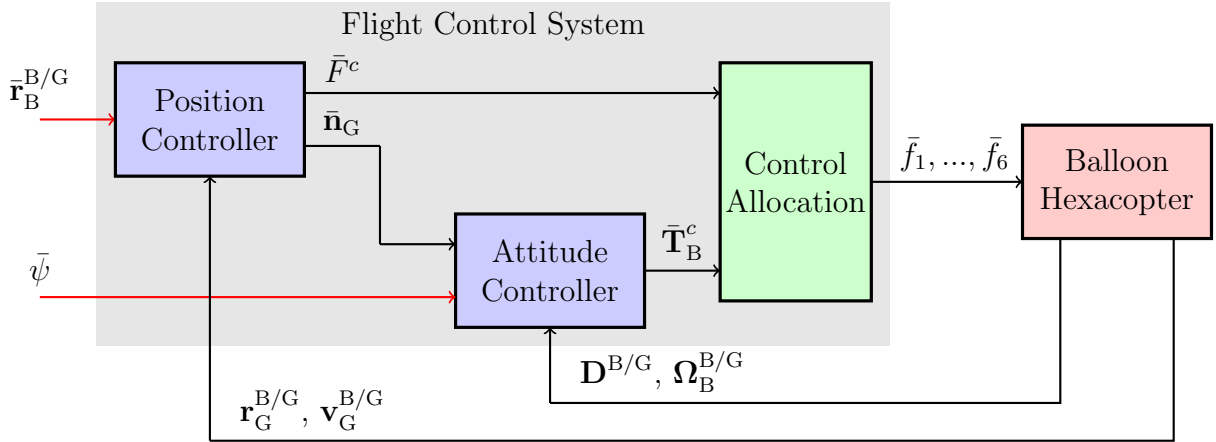


Figure 4: Architecture of the balloon-hexacopter control system.

3. Flight Control System

A hierarchical control strategy is adopted here, as illustrated in Figure 4. In this strategy, the flight control is realized by two nested control loops, where the inner loop is responsible for the attitude control, while the outer loop performs position control. The position controller receives an external position command $\bar{\mathbf{r}}_G^{B/G}$ as well as feedbacks of position $\mathbf{r}_G^{B/G}$ and velocity $\mathbf{v}_G^{B/G}$ from the vehicle. On the other hand, it produces the thrust command vector $\bar{F}^c \bar{\mathbf{n}}_G$, where $\bar{\mathbf{n}}_G$ is a two-DOF attitude command that, together with the external heading command $\bar{\psi}$, composes the three-DOF command input of the attitude controller. The latter receives feedback of the vehicle's three-dimensional attitude $\mathbf{D}^{B/G}$ and angular velocity $\mathbf{\Omega}_B^{B/G}$. The control allocation block is responsible for generating the individual thrust commands \bar{f}_i , $i = 1, \dots, 6$, from the total thrust magnitude command \bar{F}^c and torque command $\bar{\mathbf{T}}_B^c$.

3.1. Time-Scale Separation

The hierarchical control architecture considered here is the classical and ubiquitous one in the MAV control literature. It is based on the assumption that there is a time-scale separation between the closed-loop translational and rotational vehicle dynamics [2]. This assumption is ensured by tuning the attitude control loop to converge much faster than the position control loop. Under such conditions, when designing the position control law, one can assume that the actual attitude $\mathbf{D}^{B/G}$ converges to the corresponding command $\bar{\mathbf{D}}^{B/G}$ instantaneously, i.e., $\mathbf{D}^{B/G} = \bar{\mathbf{D}}^{B/G}$. On the

other hand, when designing the attitude control law, the attitude command $\bar{\mathbf{D}}^{\text{B/G}}$ is assumed to be constant, or equivalently, the angular velocity command $\bar{\boldsymbol{\Omega}}_{\text{B}}^{\text{B/G}}$ is assumed to be zero. On the basis of these assumptions, the attitude and position control laws can be designed separately as detailed in the sequel.

3.2. Attitude Control

The design model adopted for deriving the attitude control law is obtained from equation (13) by: 1) neglecting the disturbance torque, 2) replacing the actual control torque $\mathbf{T}_{\text{B}}^{\text{c}}$ by the corresponding command $\bar{\mathbf{T}}_{\text{B}}^{\text{c}}$, and 3) considering that the rotor dynamics is so fast that one can assume $\dot{\omega}_i = 0$ and $\omega_i = \bar{\omega}_i$. The resulting design model is

$$\dot{\boldsymbol{\Omega}}_{\text{B}}^{\text{B/G}} = (\mathbf{J}^b)^{-1} \left(\left[\left(\mathbf{J}^b \boldsymbol{\Omega}_{\text{B}}^{\text{B/G}} + J^r \sum_{i=1}^6 (-1)^i \bar{\omega}_i \mathbf{e}_3 \right) \times \right] \boldsymbol{\Omega}_{\text{B}}^{\text{B/G}} + [(d\mathbf{e}_3) \times] \mathbf{D}^{\text{B/G}} \begin{bmatrix} 0 \\ 0 \\ F^b \end{bmatrix} + \bar{\mathbf{T}}_{\text{B}}^{\text{c}} \right). \quad (18)$$

Suppose that the torque command $\bar{\mathbf{T}}_{\text{B}}^{\text{c}}$ is bounded from $-\mathbf{T}^{\text{max}} \in \mathbb{R}^3$ to $\mathbf{T}^{\text{max}} \triangleq [T_1^{\text{max}} T_2^{\text{max}} T_3^{\text{max}}]^{\text{T}}$.

The attitude controller proposed here is given by

$$\bar{\mathbf{T}}_{\text{B}}^{\text{c}} = \boldsymbol{\sigma}_{[-\mathbf{T}^{\text{max}}, \mathbf{T}^{\text{max}}]}(\boldsymbol{\gamma}^a), \quad (19)$$

where $\boldsymbol{\gamma}^a \triangleq [\gamma_1^a \ \gamma_2^a \ \gamma_3^a]^{\text{T}} \in \mathbb{R}^3$ is defined by

$$\boldsymbol{\gamma}^a \triangleq -[(d\mathbf{e}_3) \times] \mathbf{D}^{\text{B/G}} \begin{bmatrix} 0 \\ 0 \\ F^b \end{bmatrix} + [\boldsymbol{\Omega}_{\text{B}}^{\text{B/G}} \times] \mathbf{J}^b \boldsymbol{\Omega}_{\text{B}}^{\text{B/G}} + J^r [\boldsymbol{\Omega}_{\text{B}}^{\text{B/G}} \times] \mathbf{e}_3 \sum_{i=1}^6 (-1)^i \bar{\omega}_i + \mathbf{J}^b \mathbf{K}_1 \boldsymbol{\varepsilon} - \mathbf{J}^b \mathbf{K}_2 \boldsymbol{\Omega}_{\text{B}}^{\text{B/G}}, \quad (20)$$

where $\boldsymbol{\varepsilon} \in \mathbb{R}^3$ are the Euler angles (1-2-3 sequence) corresponding to the attitude control error

$\tilde{\mathbf{D}} = \bar{\mathbf{D}}^{\text{B/G}}(\mathbf{D}^{\text{B/G}})^{\text{T}}$, $\mathbf{K}_1, \mathbf{K}_2 \in \mathbb{R}^{3 \times 3}$ are the controller gains, and

$$\boldsymbol{\sigma}_{[-\mathbf{T}^{\text{max}}, \mathbf{T}^{\text{max}}]}(\boldsymbol{\gamma}^a) \triangleq \begin{bmatrix} \sigma_{[-T_1^{\text{max}}, T_1^{\text{max}}]}(\gamma_1^a) \\ \sigma_{[-T_2^{\text{max}}, T_2^{\text{max}}]}(\gamma_2^a) \\ \sigma_{[-T_3^{\text{max}}, T_3^{\text{max}}]}(\gamma_3^a) \end{bmatrix}, \quad (21)$$

$$\sigma_{[-T_l^{\text{max}}, T_l^{\text{max}}]}(\gamma_l^a) \triangleq \begin{cases} -T_l^{\text{max}}, & \gamma_l < -T_l^{\text{max}} \\ \gamma_l, & \gamma_l \in [-T_l^{\text{max}}, T_l^{\text{max}}] \\ T_l^{\text{max}}, & \gamma_l > T_l^{\text{max}} \end{cases}, \quad l = 1, 2, 3. \quad (22)$$

Note that the proposed attitude control law (19) is such that, if no saturation is active, it cancels the first and second term on the right-hand side of equation (18), remaining a feedback-linearized closed-loop dynamics controlled by the proportional-derivative actions appearing in the last two terms of equation (20).

3.3. Position Control

Here, the design model is obtain from equation (17), by assuming that: 1) the disturbance force \mathbf{F}_G^d is negligible, 2) the actual control force magnitude F^c is identical to the corresponding command \bar{F}^c , and 3) $\mathbf{D}^{\text{B/G}} = \bar{\mathbf{D}}^{\text{B/G}}$ (time-scale separation). The resulting design model is

$$\ddot{\mathbf{r}}_G^{\text{B/G}} = \mathbf{M}^{-1} \bar{\mathbf{F}}_G^c + \begin{bmatrix} 0 \\ 0 \\ Vg(\rho_{\text{air}} - \rho_{\text{helium}})/m^t - g \end{bmatrix}, \quad (23)$$

where $\bar{\mathbf{F}}_G^c = \bar{F}^c \bar{\mathbf{n}}_G \in \mathbb{R}^3$ is the control force command and $\bar{\mathbf{n}}_G \in \mathbb{R}^3$ is the transpose of the third line of $\bar{\mathbf{D}}^{\text{B/G}}$.

Suppose that $\bar{\mathbf{F}}_G^c$ is bounded within a parallelepipedal set from $\mathbf{F}^{\text{min}} \triangleq [F_1^{\text{min}} \ F_2^{\text{min}} \ F_3^{\text{min}}]^{\text{T}} \in \mathbb{R}^3$ to $\mathbf{F}^{\text{max}} \triangleq [F_1^{\text{max}} \ F_2^{\text{max}} \ F_3^{\text{max}}]^{\text{T}} \in \mathbb{R}^3$. The position controller proposed here is given by

$$\bar{\mathbf{F}}_G^c = \boldsymbol{\sigma}_{[\mathbf{F}^{\text{min}}, \mathbf{F}^{\text{max}}]}(\boldsymbol{\gamma}^p), \quad (24)$$

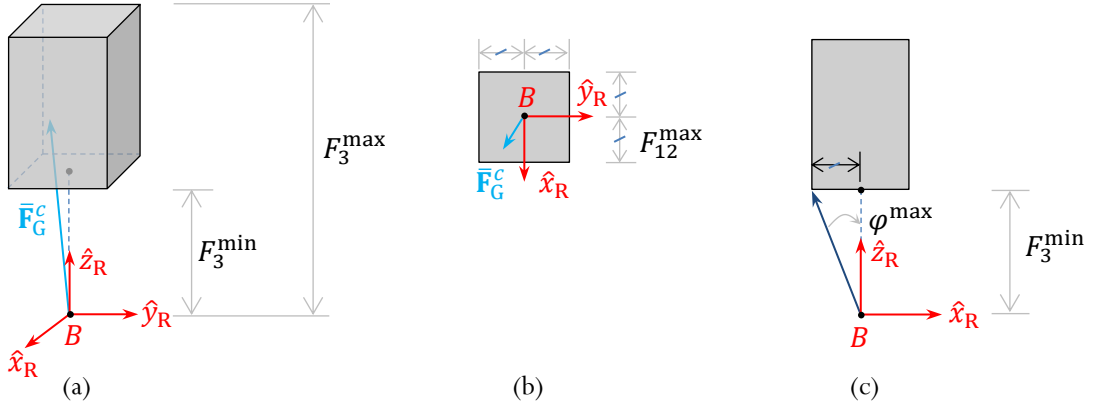


Figure 5: Constraint set of the position control input. (a) Perspective view showing the control force command inside the parallelepipedal set. (b) Superior view showing the bounds $F_1^{\max} = F_2^{\max} = F_{12}^{\max}$. (c) Lateral view showing the maximum inclination angle φ^{\max} .

where

$$\gamma^p \triangleq - \begin{bmatrix} 0 \\ 0 \\ Vg(\rho_{\text{air}} - \rho_{\text{helium}}) - m^t g \end{bmatrix} + \mathbf{MK}_3 \left(\bar{\mathbf{r}}_G^{\text{B/G}} - \mathbf{r}_G^{\text{B/G}} \right) - \mathbf{MK}_4 \dot{\mathbf{r}}_G^{\text{B/G}} \quad (25)$$

and the saturation function $\sigma_{[\mathbf{F}^{\min}, \mathbf{F}^{\max}]}(\cdot)$ is as defined in equations (21)-(22). The matrices $\mathbf{K}_3, \mathbf{K}_4 \in \mathbb{R}^{3 \times 3}$ are the controller gains.

Note that the proposed controller (24) is such that, if no saturation is active, it cancels the second term on the right-hand side of equation (23), remaining a double-integrator closed-loop dynamics controlled by the proportional-derivative actions appearing in the last two terms of equation (25). In saturation-free conditions, it is straightforward to show asymptotic stability of the proposed translational control loop using linear time-invariant control methods.

By constraining the control input $\bar{\mathbf{F}}_G^c$ inside a parallelepipedal set, one can deal with bounds on its magnitude \bar{F}^c as well as on its inclination angle w.r.t. the local vertical. To illustrate it, define a reference CCS S_R with origin at B whose axes are parallel to S_G , as depicted in Figure 5. From the geometry of the constraint set, one can see that $F_1^{\min} = -F_1^{\max}$, $F_2^{\min} = -F_2^{\max}$, and $F_1^{\max} = F_2^{\max} = F_{12}^{\max} = F_3^{\min} \tan \varphi^{\max}$, where φ^{\max} is the maximum allowed inclination angle of $\bar{\mathbf{F}}_G^c$ w.r.t. \hat{z}_R .

3.4. Control Allocation

Equation (5) related the true resultant efforts F^c and \mathbf{T}_B^c with the six individual effector forces compacted in \mathbf{f} . One can induce that the respective effort commands are interrelated by

$$\begin{bmatrix} \bar{F}^c \\ \bar{\mathbf{T}}_B^c \end{bmatrix} = \mathbf{\Gamma} \bar{\mathbf{f}}, \quad (26)$$

where $\bar{\mathbf{f}} \triangleq [\bar{f}_1 \ \bar{f}_2 \ \dots \ \bar{f}_6]^T$.

The control allocation pursued here consists in a solution $\bar{\mathbf{f}}$ of the system of linear equations (26). Since this is an undetermined system (with infinity solutions), we choose here the one that solves the optimization problem:

$$\min \|\bar{\mathbf{f}}\|^2 \quad (27)$$

subject to the equality constraint (26). The explicit solution to this problem can be immediately found by using Lagrange multipliers. It is

$$\bar{\mathbf{f}} = \mathbf{\Gamma}^T (\mathbf{\Gamma} \mathbf{\Gamma}^T)^{-1} \begin{bmatrix} \bar{F}^c \\ \bar{\mathbf{T}}_B^c \end{bmatrix}. \quad (28)$$

One can easily verify that (28) is a solution of (26). In particular, this is the solution that minimizes the square of the Euclidian norm of $\bar{\mathbf{f}}$ and, therefore, it is the one that spends less energy.

4. Deterministic Evaluation

As a first step of evaluation of the proposed method, this section presents a deterministic simulation of the proposed flight control system. Subsection 4.1 describes the simulation and shows the adopted nominal parameters, while Subsection 4.2 presents and analyzes the simulation results.

It is worth noting at this point that both the aerostatic lift F^b and the restoring torque \vec{T}^b depend on the value of ρ_{air} and ρ_{helium} . These densities in turn depend on the local temperature and pressure, as expressed in the Ideal Gas Law:

$$\rho_q = \frac{p}{R_q T}, \quad (29)$$

where “q” can be replaced by either “air” or “helium”, p is the local pressure in Pa, T is the local temperature in K, and R_q is the specific gas constant ($R_{\text{air}} = 286.9$ J/Kg/K and $R_{\text{helium}} = 2077$ J/Kg/K). In particular, in this section, the local temperature and pressure are assumed to be constant with values 20°C and 89871.07 Pa. Under such conditions, the air and helium densities are calculated to be $\rho_{\text{air}} \approx 1.0686$ kg/m³ and $\rho_{\text{helium}} \approx 0.1476$ kg/m³. These values are used here to simulate the ground truth as well as to compute the control laws.

4.1. Plant and Controller Parameters

For simulating the overall closed-loop flight control system illustrated in Figure 4, we use the models formulated in Section 2 as well as the control laws and control allocation proposed in Section 3. Table 1 shows the values of the balloon-hexacopter parameters that we assume to be deterministic in the present study. On the other hand, Table 2 presents the adopted controller parameters. The controller gains are tuned by trial and error, taking into account their proportional or derivative effect and considering the time-scale separation assumption as well.

Table 1: Deterministic parameters of the plant.

Description	Symbol	Value
Force coefficient	k_f	1.2838×10^{-5} N/(rad/s) ²
Torque coefficient	k_τ	3.0811×10^{-7} Nm/(rad/s) ²
Maximum rotor speed	$\bar{\omega}_{\max}$	906.66 rad/s
Motor speed coefficient	k_ω	1
Motor time constant	τ_ω	0.01 s
Arm length	l	1 m
Volume of the balloon	V	5.3 m ³
CB-CM displacement	d	0.85 m
Total inertia matrix	\mathbf{J}^b	diag(0.1, 0.1, 0.2) Kgm ²
Moment of inertia of the rotors	J^r	0.005 Kgm ²
Total empty mass	m^t	9.392 Kg

In this paper, for obtaining simulation data that are consistent with a typical operation of MAVs, the proposed flight control system is commanded to follow a waypoint-based position

Table 2: Parameters of the attitude and position control laws.

Description	Symbol	Value
Proportional gain of the attitude controller	\mathbf{K}_1	diag(200, 200, 200)
Derivative gain of the attitude controller	\mathbf{K}_2	diag(120, 120, 120)
Proportional gain of the position controller	\mathbf{K}_3	diag(20, 20, 20)
Derivative gain of the position controller	\mathbf{K}_4	diag(20, 20, 20)
Maximum torque command	\mathbf{T}^{\max}	$[13.52 \ 11.70 \ 0.56]^T$ Nm
Minimum force command	\mathbf{F}^{\min}	$[-6.97 \ -6.97 \ 2.60]^T$ N
Maximum force command	\mathbf{F}^{\max}	$[6.97 \ 6.97 \ 52.02]^T$ N
Maximum inclination angle	φ^{\max}	15 degrees

trajectory. In this trajectory, the waypoints are connected by straight lines with length of 5 m and constant desired velocity of $\bar{v} = 0.5$ m/s. Moreover, the heading angle command $\bar{\psi}$ is set to zero.

4.2. Deterministic Simulation Results

Figures 6–8 are the results of the deterministic simulation using the parameters of Table 1–2. Figure 6 shows the effective position and the corresponding position command. In the ramp part of the component trajectories, one can verify a steady-state error of about 0.5 m. After finishing the ramp commands, the overshoot and accommodation time (of 5 cm around the final value) are approximately 5 mm and 2 s, respectively.

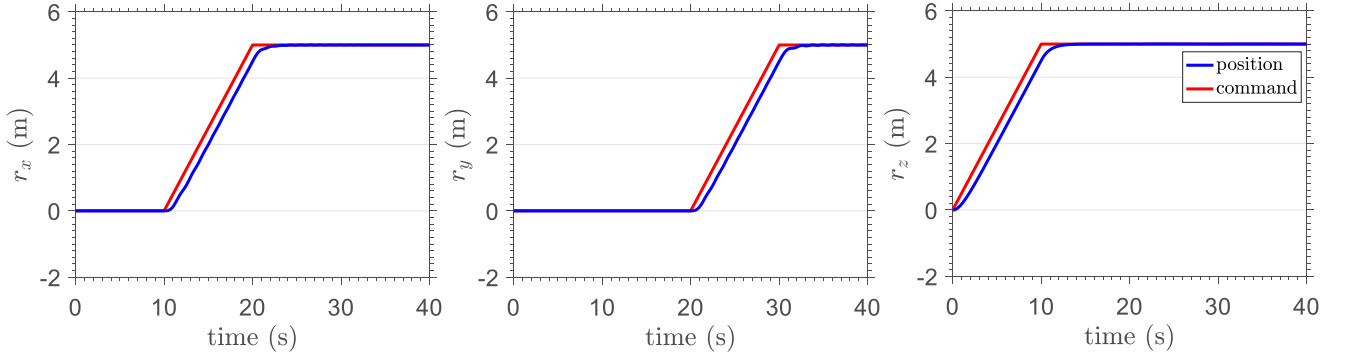


Figure 6: Deterministic performance of the position control.

Figure 7 shows the performance of the attitude control loop. The attitude pitch and roll commands oscillate at the waypoints and the corresponding true attitude angles follow them with an apparently slow and attenuated response. However, this performance is sufficient for obtaining

the good position tracking result shown in Figure 6. In the pitch and roll plots, one can also see that the force bounds ($\mathbf{F}^{\min}, \mathbf{F}^{\max}$) of the position control law put limits of about 15 degrees on the inclination of the force command with respect to the local vertical.

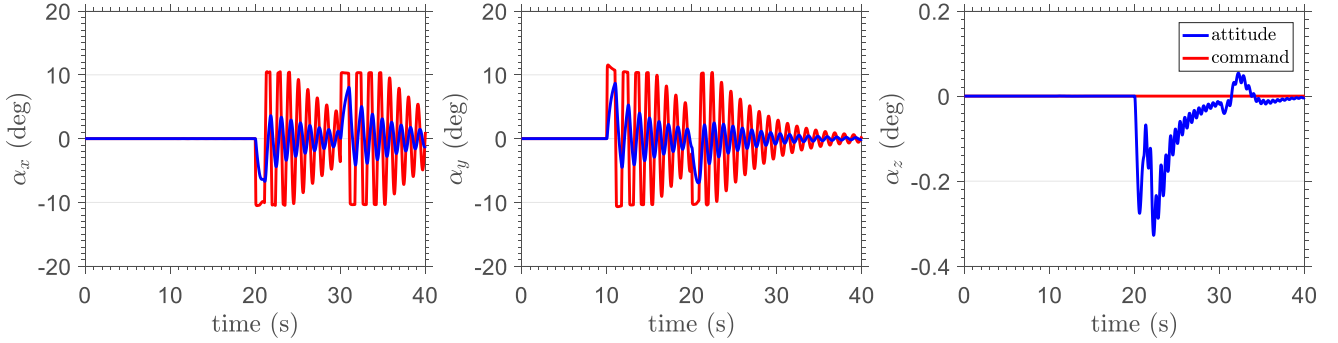


Figure 7: Deterministic performance of the attitude control.

Finally, Figure 8 shows the components of the torque command $\bar{\mathbf{T}}_B^c$ generated by the attitude controller and Figure 9 presents the force magnitude command \bar{F}^c computed by the position controller. The force command \bar{F}^c does not reach its maximum bound, even in the beginning part of the trajectory, from 0 to 10 s, where the vehicle is command to ascend. After the transients caused by the maneuvers at the waypoints, \bar{F}^c seems to converge and stay around 41.25 N, which is equivalent to the total weigh of the vehicle and payload minus the aerostatic lift. On the other hand, the \hat{x}_B and \hat{y}_B components of the torque command $\bar{\mathbf{T}}_B^c$ start a damped oscillatory behavior at the waypoints for attenuating the oscillation in the attitude roll and pitch angles. During all the simulation, the components of $\bar{\mathbf{T}}_B^c$ keep inside their bounds $\pm \mathbf{T}^{\max}$ with a large margin (see Table 2).

5. Uncertainty Quantification

The present section conducts an uncertainty quantification analysis of the flight control system under consideration using a parametric probabilistic approach [15, 16]. In this analysis, the temperature and pressure are modeled as independent uniform random variables and, based on these random models, for each flight realization, one new outcome is generated for both variables.

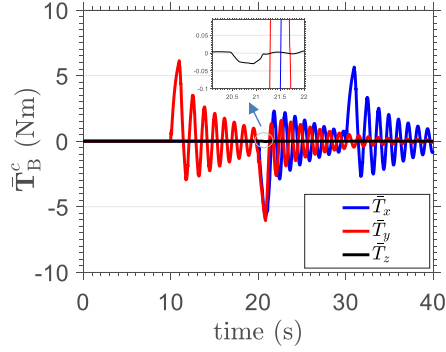


Figure 8: Torque command in the deterministic simulation.

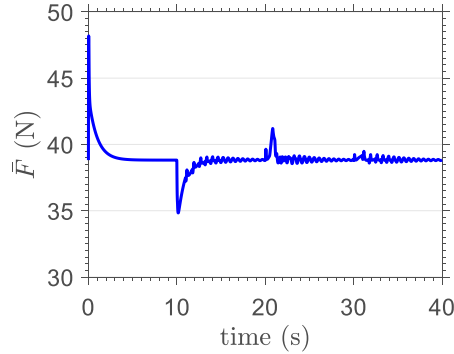


Figure 9: Force magnitude command in the deterministic simulation.

5.1. Probabilistic Model

Let $(\Theta, \Sigma, \mathbb{P})$ be a probability space, where Θ is the sample space, Σ is a σ -algebra over Θ , and $\mathbb{P} : \Sigma \rightarrow [0, 1]$ a probability measure. In this stochastic framework, the local temperature T^l and pressure P^l are modeled by (independent) random variables $\mathbb{X} : \Sigma \rightarrow \mathbb{R}$ and $\mathbb{Y} : \Sigma \rightarrow \mathbb{R}$, respectively. We assume that these random variables, whose probability distributions are $P_{\mathbb{X}}(dx)$ and $P_{\mathbb{Y}}(dy)$, admit probability density functions (PDF) $x \mapsto p_{\mathbb{X}}(x)$, with respect to dx , and $y \mapsto p_{\mathbb{Y}}(y)$, with respect to dy .

The maximum entropy principle [17] is adopted here as a way to specify the aforementioned distributions. This approach provides the least biased distributions in a scenario with little (or no) experimental information on a particular random variable [15]. In the present investigation, the random local temperature \mathbb{X} and local pressure \mathbb{Y} are both completely unknown beforehand. However, one should better specify for them reasonable operational ranges, from which it is possible

to immediately define the underlying supports. In this way, we assume from now on that \mathbb{X} and \mathbb{Y} take values in known positive finite intervals $[x_1, x_2] \subset (0, +\infty)$ and $[y_1, y_2] \subset (0, +\infty)$, respectively. Therefore, the maximum entropy principle is formulated here as the maximization of the Shannon entropies

$$\mathbb{S}(p_{\mathbb{X}}) = - \int_{\mathbb{R}} \ln p_{\mathbb{X}}(x) p_{\mathbb{X}}(x) dx \quad \text{and} \quad \mathbb{S}(p_{\mathbb{Y}}) = - \int_{\mathbb{R}} \ln p_{\mathbb{Y}}(y) p_{\mathbb{Y}}(y) dy. \quad (30)$$

of \mathbb{X} and \mathbb{Y} , subject to the normalization constraints (which bring information about the supports)

$$\int_{x_1}^{x_2} p_{\mathbb{X}}(x) dx = 1 \quad \text{and} \quad \int_{y_1}^{y_2} p_{\mathbb{Y}}(y) dy = 1. \quad (31)$$

By using the Lagrange multiplier method, one can solve the above optimization problem to obtain the following PDFs:

$$p_{\mathbb{X}}(x) = \mathbb{1}_{[x_1, x_2]}(x) \frac{1}{x_2 - x_1} \quad \text{and} \quad p_{\mathbb{Y}}(y) = \mathbb{1}_{[y_1, y_2]}(y) \frac{1}{y_2 - y_1}, \quad (32)$$

where $\mathbb{1}_X(x)$ denotes the indicator function of the set X . Note that the above PDFs correspond to uniform distributions on the intervals $[x_1, x_2]$ and $[y_1, y_2]$, respectively. Informally, the above result makes all sense, because since the minimum and maximum values are the only known information about the random parameters, the most reasonable choice for their distributions is the one that assigns equal weight to all their possible values.

Due to the randomness of \mathbb{X} and \mathbb{Y} , the air density ρ_{air} and the helium density ρ_{helium} are also random variables [see equation (29)]. Further, since the aerostatic lift [see equation (7)] and the restoring torque [see equation (9)] depends on ρ_{air} and ρ_{helium} , then the rotational (13) and translational (17) dynamic models are rather differential equations with random parameters and their variables are stochastic processes. In particular, we choose here the minimum temperature $x_1 = 0^\circ \text{ C}$, the maximum temperature $x_2 = 40^\circ \text{ C}$, the minimum pressure $y_1 = 0.7739 \text{ atm}$ (at 2000 m and 0° C), and the maximum pressure $y_2 = 1 \text{ atm}$.

5.2. Propagation of Uncertainties

To compute the propagation of uncertainties of the random parameters \mathbb{X} and \mathbb{Y} through the control system dynamics, we employ the Monte Carlo (MC) method [18]. It consists in a stochastic solver that, based on n_s realizations of the random parameters \mathbb{X} and \mathbb{Y} , generates n_s different realizations of the deterministic closed-loop dynamics and computes the sample statistics of the respective system responses. These statistics are then used to approximate the solution (or response) of the original stochastic system.

In order to guarantee the convergence of the MC solution to the true stochastic behavior of the system, a sufficient number n_s of realizations must be considered. The reference [19] shows that such a convergence occurs in the mean-square sense if the following metrics converge in the pointwise sense:

$$\delta^p = \left(\frac{1}{n_s} \sum_{n=1}^{n_s} \int_{t=0}^{t_f} \left(\|\mathbf{r}_G^{\text{B/G}}(t, n)\|^2 \right) dt \right)^{1/2}, \quad (33)$$

$$\delta^a = \left(\frac{1}{n_s} \sum_{n=1}^{n_s} \int_{t=0}^{t_f} \left(\|\boldsymbol{\alpha}^{\text{B/G}}(t, n)\|^2 \right) dt \right)^{1/2}, \quad (34)$$

where n denotes an arbitrary MC realization, t denotes the continuous time, t_f is the final simulation instant, $\mathbf{r}_G^{\text{B/G}}(t, n)$ is the n th realization of the vehicle's position at instant t , and $\boldsymbol{\alpha}^{\text{B/G}}(t, n)$ is the n th realization of the vehicle's attitude (in Euler angles 1-2-3) at instant t . Figure 10 shows a plot of the position (33) and attitude (34) convergence metrics as a function of n_s . One can see that after 50 realizations, both metrics show to converge. Therefore, in the problem under consideration, we consider $n_s = 100$, which is sufficient for the convergence of the MC solution.

Figure 11 shows the position statistics. One can see that there is a very small variation in the position control performance as a consequence of the randomness of the temperature and pressure conditions. In particular, the largest uncertainties (with a confidence level of 95%), which occurs at the end of the time-ramp parts of the waypoint trajectory, reach overshoots of 20 cm in \hat{x}_G , 10 cm in \hat{y}_G and about 4 cm in \hat{z}_G . Figure 12 shows the statistics of the attitude control error. Different from the position results, the attitude errors exhibit a considerable variation, as depicted by the confidence level band, after the first waypoint, when the vehicle is commanded to translate

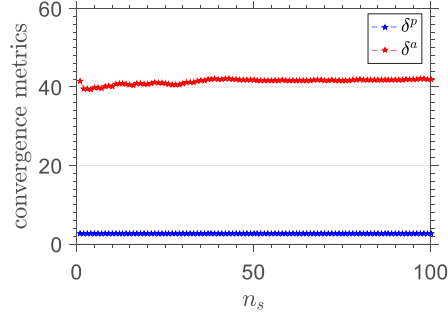


Figure 10: Convergence metrics for choosing the number of Monte Carlo realizations.

on the horizontal plane. The attitude error reaches (with a confidence level of 95%) the values of 17.7 degrees in roll, 18.7 degrees in pitch, and 0.52 degree in yaw.

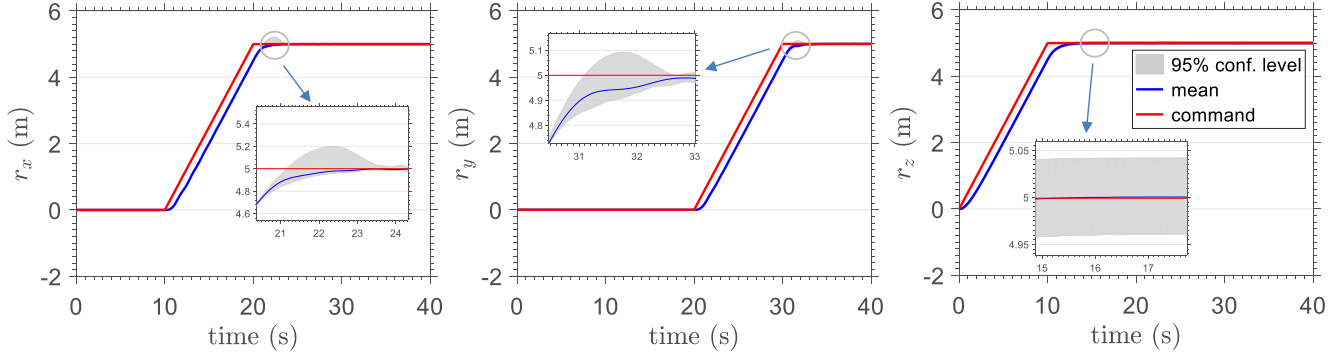


Figure 11: Position statistics of the Monte Carlo simulation.

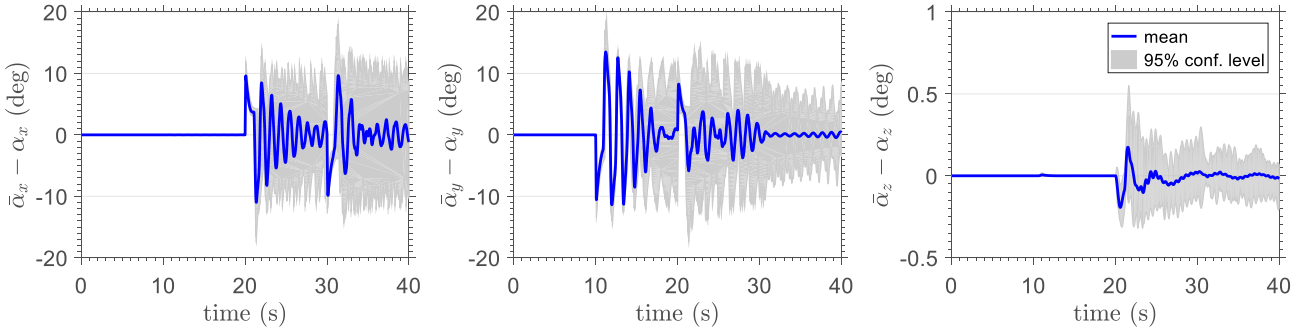


Figure 12: Attitude control error statistics of the Monte Carlo simulation.

Figure 13 shows the torque command statistics. One can observe a significantly variation in the torque command components. However, their maximum values (with a confidence level of 95%)

keep inside their bounds $\pm \mathbf{T}^{\max}$. On the other hand, Figure 14 presents the statistics of the force magnitude command. In the second of flight, when the vehicle is command to move upwards, the confidence band touches the force bounds \mathbf{F}^{\max} , even though the mean value of \bar{F}^c keeps below its bound with a reasonable margin. After this transient, \bar{F}^c does not saturate again, but, with 95% of confidence, its margin with respect to the force bound is severely reduced. In particular, it is worth noting that in the transient of the second waypoint (about 20 s), this margin was critically reduced. Finally, one can observe in Figure 15 that the variation in \bar{F}^c is a direct consequence of the variation in the aerostatic lift F^b ; within its admissibility interval the force command is capable of reacting to the variation in F^b .

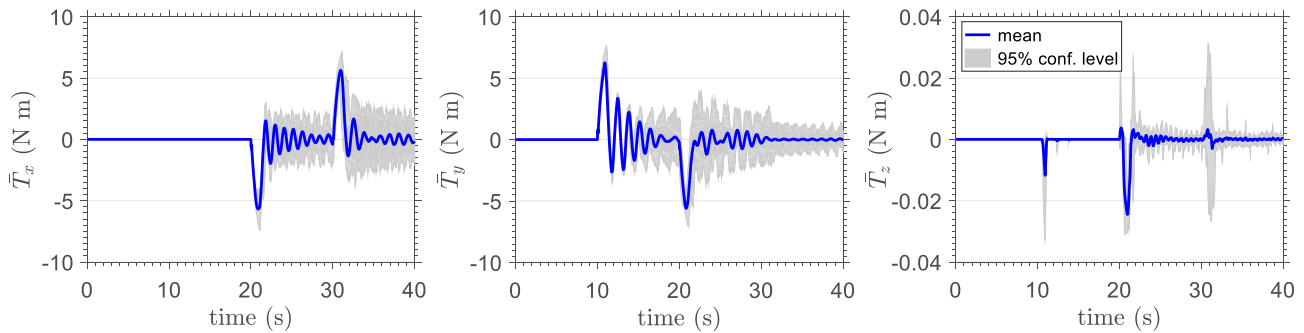


Figure 13: Torque command statistics of the Monte Carlo simulation.

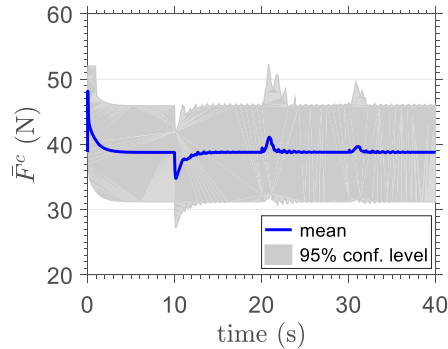


Figure 14: Force magnitude command statistics of the Monte Carlo simulation.

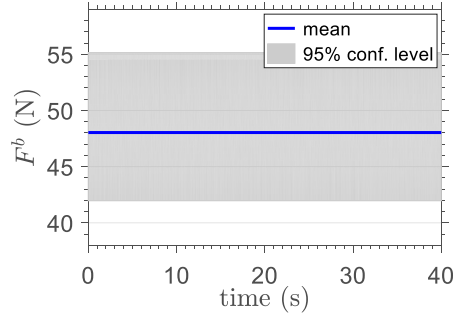


Figure 15: Aerostatic lift statistics of the Monte Carlo simulation.

6. Concluding Remarks

The paper proposed a flight control system for a new micro aerial vehicle (MAV) resulting from the combination of a hexacopter airframe with a balloon filled with helium. This MAV is a straightforward attempt to extend the flight duration and load capacity of conventional multirotor vehicles by means of an aerostatic lift. On one hand, such a combination results in a very simple vehicle. On the other hand, even for indoor flight, its control system must be carefully designed to overcome the effects of a restoring torque (which does not occur in conventional multirotor vehicles), while being robust to variations in the local temperature and pressure operation conditions. The proposed flight control system is evaluated on the basis of both deterministic and stochastic simulations. In particular, the deterministic simulation shows that in nominal conditions, it is possible to control the vehicle's position to follow a desired waypoint-based trajectory with reference speed of 0.5 m/s. The obtained performance is sufficient accurate and fast for many MAV applications. On the other hand, in the stochastic simulation, the local temperature and pressure are modeled by uniformly-distributed random variables and the resulting performance is rigorously evaluated by Monte Carlo (MC) simulation. The variability verified in the position control performance can be considered small enough to dispense a special design of the control laws in order to suppress it. However, the variability shown in the attitude control error motivates a special robust control method for a better performance of the system in a stochastic sense.

Acknowledgment

The authors would like to thank all those people who indirectly contributed or motivated us to conduct the present investigation. In special, we are grateful to Mr. Luciano S. Araujo (from Elio Tecnologia), who designed and built the first prototype of the balloon-hexacopter and donated it to the Laboratório de Robótica Aérea do ITA.

References

- [1] R. Mahony, V. Kumar, P. Corke, Multirotor Aerial Vehicles: Modeling, Estimation, and Control of Quadrotor, *IEEE Robotics & Automation Magazine* 19 (3) (2012) 20–32. doi:10.1109/MRA.2012.2206474.
- [2] S. Bertrand, N. Guénard, T. Hamel, H. Piet-Lahanier, L. Eck, A hierarchical controller for miniature VTOL UAVs: Design and stability analysis using singular perturbation theory, *Control Engineering Practice* 19 (10) (2011) 1099–1108. doi:10.1016/j.conengprac.2011.05.008.
- [3] S. Bouabdallah, A. Noth, R. Siegwart, PID vs LQ control techniques applied to an indoor micro quadrotor, 2004 IEEE/RSJ International Conference on Intelligent Robots and Systems (IROS) (IEEE Cat. No.04CH37566) 3 (2004) 2451–2456. doi:10.1109/IROS.2004.1389776. URL <http://ieeexplore.ieee.org/document/1389776/>
- [4] P. Castillo, R. Lozano, A. Dzul, Stabilization of a Mini Rotorcraft with Four Rotors, *IEEE Control Systems Magazine* (December) (2005) 45–55. doi:10.1109/IROS.2004.1389815.
- [5] A. Tayebi, S. McGilvray, Attitude stabilization of a VTOL quadrotor aircraft, *IEEE Transactions on Control Systems Technology* 14 (3) (2006) 562–571. doi:10.1109/TCST.2006.872519.
- [6] R. Cunha, D. Cabecinhas, C. Silvestre, Nonlinear trajectory tracking control of a quadrotor vehicle, in: *Proceedings of the European Control Conference, Budapest, 2009*, pp. 2763–2768. URL <http://users.isr.ist.utl.pt/~pjcro/courses/dsfps0910/docs/prts/DavidCabecinhas-ECC2009paper.pdf>
- [7] T. Lee, M. Leok, N. H. McClamroch, Geometric Tracking Control of a Quadrotor UAV on $SE(3)$, in: *49th IEEE Conference on Decision and Control, Atlanta, 2010*, pp. 5420–5425. arXiv:arXiv:1003.2005v1, doi:10.1002/asjc.567. URL <http://doi.wiley.com/10.1002/asjc.567>http://ieeexplore.ieee.org/xpls/abs_all.jsp
- [8] D. A. Santos, O. Saotome, A. Cela, Trajectory control of multirotor helicopters with thrust vector constraints, in: *2013 21st Mediterranean Conference on Control and Au-*

tomation, MED 2013 - Conference Proceedings, Platania-Chania, 2013, pp. 375–379. doi:10.1109/MED.2013.6608749.

- [9] I. A. A. Prado, D. A. Santos, A safe position tracking strategy for multirotor helicopters, in: 2014 22nd Mediterranean Conference on Control and Automation, MED 2014, Palermo, 2014, pp. 1433–1439. doi:10.1109/MED.2014.6961577.
- [10] J. Yan, D. A. Santos, D. S. Bernstein, Adaptive control with convex saturation constraints, IET Control Theory & Applications 8 (12) (2014) 1096–1104. doi:10.1049/iet-cta.2013.0528. URL <http://digital-library.theiet.org/content/journals/10.1049/iet-cta.2013.0528>
- [11] L. Besnard, Y. B. Shtessel, B. Landrum, Quadrotor vehicle control via sliding mode controller driven by sliding mode disturbance observer, Journal of the Franklin Institute 349 (2) (2012) 658–684. doi:10.1016/j.jfranklin.2011.06.031.
- [12] T. Lee, M. Leok, N. H. McClamroch, Nonlinear robust tracking control of a quadrotor UAV on $SE(3)$, Asian Journal of Control 15 (2) (2013) 391–408. arXiv:arXiv:1003.2005v1, doi:10.1002/asjc.567.
- [13] E.-H. Zheng, J.-J. Xiong, J.-L. Luo, Second order sliding mode control for a quadrotor UAV, ISA transactions 53 (4) (2014) 1–7. doi:10.1016/j.isatra.2014.03.010. URL <http://www.ncbi.nlm.nih.gov/pubmed/24751475>
- [14] R. López-Gutiérrez, A. E. Rodríguez-Mata, S. Salazar, I. González-Hernández, R. Lozano, Robust Quadrotor Control: Attitude and Altitude Real-Time Results, Journal of Intelligent & Robotic Systems doi:10.1007/s10846-017-0520-y. URL <http://link.springer.com/10.1007/s10846-017-0520-y>
- [15] C. Soize, Stochastic modeling of uncertainties in computational structural dynamics - recent theoretical advances, Journal of Sound and Vibration 332 (10) (2013) 2379 – 2395. doi:<http://dx.doi.org/10.1016/j.jsv.2011.10.010>.
- [16] C. Soize, Uncertainty Quantification: An Accelerated Course with Advanced Applications in Computational Engineering, Springer, 2017.

- [17] E. T. Jaynes, Information theory and statistical mechanics, *Physical Review Series II* 106 (1957) 620–630. doi:10.1103/PhysRev.106.620.
- [18] R. Y. Rubinstein, D. P. Kroese, *Simulation and the Monte Carlo Method*, 3rd Edition, Wiley, 2016.
- [19] C. Soize, A comprehensive overview of a non-parametric probabilistic approach of model uncertainties for predictive models in structural dynamics, *Journal of Sound and Vibration* 288 (2005) 623–652. doi:10.1016/j.jsv.2005.07.009.